Geophys. J. Int. (2006) **165,** 135–148 doi: 10.1111/j.1365-246X.2006.02834.x

Impact of fabric, microcracks and stress field on shale anisotropy

David N. Dewhurst and Anthony F. Siggins

CSIRO Petroleum, Australian Petroleum Co-operative Research Centre, 26 *Dick Perry Avenue, Kensington, WA* 6151, *Australia.*
E-mail: david.dewhurst@csiro.au

Accepted 2005 October 10. Received 2005 October 4; in original form 2004 December 21

SUMMARY

Few data are available on shales in terms of seismic to ultrasonic properties and anisotropy, although all are important with regards to imaging problems often encountered in such lithologies. Additionally, mechanisms causing changes in these properties are not well documented due to the fine grain size of such materials and time required for testing under controlled pore pressure conditions. The results presented here are derived from a set of experiments run on Muderong Shale with pore pressure control in order to evaluate the effect of stress magnitude and stress anisotropy on ultrasonic response. This shale was noted to have a linear velocity-mean effective stress response and extremely high anisotropy, both likely the result of the presence of fluid-filled cracks in a low- permeability porous medium. Changes in velocity and V_p/V_s ratios are dependent on both stress and smectite content. *S*-wave velocity is significantly affected by the presence of smectite in this and other shales and at low stress (<20 MPa) is less sensitive to stress change than *P*-wave velocity. V_p/V_s ratios are noted to increase in this shale up to 20 MPa effective stress, then decrease slightly due to stress-induced loss of interlayer water in smectite. Intrinsic anisotropy comes from composition, a strong compaction fabric and the presence of microfractures; changes to ultrasonic anisotropy are the result of the magnitude of the stresses, their orientation with respect to the fractures and the degree of stress anisotropy.

Key words: shale, smectite, stress, stress anisotropy, velocity anisotropy.

INTRODUCTION

Shales are the dominant clastic component in sedimentary basins, providing seals and flow barriers on timescales relevant to both exploration (millions of years) and production (days to years). However, our understanding of their dynamic elastic behaviour is limited, due in part to lack of well-preserved samples (see Wang 2002a) and also to the time involved for testing due to their low permeability (e.g. Katsube *et al.* 1991; Dewhurst *et al.* 1998, 1999a,b). In addition, many velocity measurements acquired on shales have been made without control of pore pressure, which is critical if relating velocities to changes in effective stress conditions. Shale anisotropy has been known to be a significant problem for many years in terms of depth conversion for seismic exploration (e.g. Banik 1984; Thomsen 1986), imaging of structures in both seismic and cross-hole tomography domains (e.g. Carrion *et al.* 1992; Meadows & Abriel 1994) and also for amplitude variation with offset (AVO) analysis (e.g. Wright 1987). This latter technique can be used for gas identification (e.g. Sheriff 2002) but failure to account for anisotropy may lead to mis-identification of fluid type. In addition, anisotropy can cause significant error in estimating dynamic Poisson's ratio (Thomsen 1986). Few laboratory determinations of the full elastic tensor and resultant anisotropy have been made for shales (e.g. Jones & Wang 1981; Vernik & Nur 1992; Johnston & Christensen 1994, 1995; Vernik & Landis 1996; Hornby 1998; Jakobsen & Johansen 2000; Domnesteanu *et al.* 2002; Wang 2002a) and many of these had no pore pressure control or were unsaturated. Such studies generally show shales to be transversely isotropic (TI; e.g. Jones & Wang 1981; Vernik & Nur 1992; Wang 2002a,b), with the degree of anisotropy dependent on a number of factors such as porosity, kerogen content and microfractures. High anisotropy is noted for example in tight, low-porosity organic shales (Vernik & Liu 1997). Stress effects in shale overburden as a result of reservoir depletion also have a significant effect on time-lapse (4-D) seismic response in these low-permeability rocks and are not well understood at present (e.g. Hatchell *et al.* 2003; Kenter *et al.* 2004; Molenaar *et al.* 2004).

Factors affecting velocity and anisotropy in shales include stress state, stress history, smectite content, organic content, microstructure and physicochemical interactions with pore fluids (e.g. Holt *et al.* 1991; Vernik & Liu 1997). While it is difficult to know all these parameters *in situ*, controlled laboratory experiments on well-characterized shales under *in situ* stress and pore pressure conditions can shed light on the influence of some of these factors on shale velocity and anisotropic response. This study investigates the ultrasonic response of well-characterized Muderong Shale, a regional top seal on the Northwest Shelf of Australia, to changing stress and pore pressure conditions.

TERMINOLOGY

Recent developments in integrating rock physics with geomechanics has been prompted by the growth in 4-D seismic observations and the associated problems involved in interpreting changes of seismic response in the reservoir (e.g. Hatchell *et al.* 2003; Kenter *et al.* 2004; Molenaar *et al.* 2004). This drawing together of the disciplines requires some clarification of terminology, since confusing terminology is often used by seismic practitioners for certain stress conditions that have long-established conventions in both geomechanics and structural geology. In this paper, we advocate the following definitions:

(1) We define nett pressure as the difference between confining pressure (P_c) and pore pressure (P_p). This is commonly referred to as 'differential pressure' but confusing when used in conjunction with 3 below.

$$\text{Hence : } Nett\ Pressure = P_c - P_p. \tag{1}$$

(2) Effective stress (σ') is defined as total stress (σ) minus a fraction of the pore fluid pressure (P_p), that is:

$$\sigma' = \sigma - \alpha P_p, \tag{2}$$

where α is the Biot–Willis coefficient (Biot & Willis 1957). In weak rocks such as shales, α is generally close to 1 and this assumption is used in this paper.

(3) Differential stress is defined by the difference between the maximum (σ'_1) and minimum (σ'_3) principal effective stresses and essentially is a measure of stress anisotropy.

$$\text{Hence : } Differential\ stress = \sigma'_1 - \sigma'_3. \tag{3}$$

(4) Mean effective stress (σ'_m) is defined as:

$$\sigma'_m = \left(\frac{\sigma'_1 + \sigma'_2 + \sigma'_3}{3}\right), \tag{4}$$

where σ'_1, σ'_2 and σ'_3 are the maximum, intermediate and minimum principal effective stresses. In the standard triaxial tests used here, $\sigma'_2 = \sigma'_3$.

Hooke's law for an anisotropic elastic rock exhibiting vertical transverse isotropy (VTI) is given in Cartesian coordinates by:

$$\begin{bmatrix} \sigma_{xx} \\ \sigma_{yy} \\ \sigma_{zz} \\ \sigma_{yz} \\ \sigma_{xz} \\ \sigma_{xy} \end{bmatrix} = \begin{bmatrix} c_{11} & c_{12} & c_{13} & 0 & 0 & 0 \\ & c_{11} & c_{13} & 0 & 0 & 0 \\ & & c_{33} & 0 & 0 & 0 \\ & & & c_{44} & 0 & 0 \\ Symm & & & & c_{44} & 0 \\ & & & & & c_{66} \end{bmatrix} \begin{bmatrix} \varepsilon_{xx} \\ \varepsilon_{yy} \\ \varepsilon_{zz} \\ \varepsilon_{yz} \\ \varepsilon_{xz} \\ \varepsilon_{xy} \end{bmatrix}, \tag{5}$$

where z lies along the symmetry axis, c_{ij} are the elastic stiffness coefficients, $\sigma_{xx,yy,zz}$ are normal stresses, $\sigma_{zx,yz,xy}$ are shear stresses, $\varepsilon_{xx,yy,zz}$ are normal strains, and $\varepsilon_{zx,yz,xy}$ are shear strains. Velocities and elastic constants are related via the following equations:

$$V_{pv} = (c_{33}/\rho)^{1/2} \tag{6}$$

$$V_{ph} = (c_{11}/\rho)^{1/2} \tag{7}$$

$$V_{S1} = (c_{44}/\rho)^{1/2} \tag{8}$$

$$V_{sh} = ([c_{11} - c_{12}]/2\rho)^{1/2} \tag{9}$$

$$c_{13} = \left(-c_{44} + \left[4\rho^2 q V_{p45}^4 - 2\rho q V_{p45}^2 (c_{11} + c_{33} + 2c_{44}) + (c_{11} + c_{44})(c_{33} + c_{44})\right]^{1/2}\right), \tag{10}$$

where V_{pv} is the P-wave velocity along the axis of rotational symmetry (usually the bedding normal), V_{ph} is the P-wave velocity parallel to the bedding, V_{s1} is the S-wave velocity normal to the bedding with polarization parallel to bedding, V_{sh} is the S-wave velocity parallel to the bedding with polarization parallel to the bedding, qV_{p45} is the quasi P-wave phase velocity and ρ is bulk density.

The anisotropy factors ε, γ and δ, are defined following the notation of Thomsen (1986), such that:

$$\varepsilon = (c_{11} - c_{33})/2c_{33} \tag{11}$$

$$\gamma = (c_{66} - c_{44})/2c_{44} \tag{12}$$

$$\delta = \frac{(c_{13} + c_{44})^2 - (c_{33} - c_{44})^2}{2c_{33}(c_{33} - c_{44})} \tag{13}$$

where the c_{ij}'s are defined in eqs (6)–(10) above.

EXPERIMENTAL METHODOLOGY

The equipment used for shale testing comprises a high stiffness load frame, a triaxial cell and systems for cell and pore pressure control. Long-term stability of the control systems and instrumentation transducers is crucial for testing of shales due to their low permeability. The rig has independent control of pore pressure, confining pressure and axial load, to the operational upper limits of 70 MPa, 70 MPa and 400 MPa, respectively. The inner diameter of the cell is considerably larger than the sample, allowing the installation of internal instruments such as a load cell, radial and axial displacement transducers, acoustic transducers and temperature sensors. The sample stack assembly includes:

(1) A specimen mounted between top and base platens, encased in a flexible, impermeable Viton membrane (0.75 mm thick), separating the confining fluid from the specimen,

(2) Two steel platens housing ultrasonic P- and S-wave elements with provision for pore pressure measurement at both ends of the specimen. Shallow grooves are engraved on the platen surfaces to distribute pore fluid evenly and allow testing without using a porous disk. The diameter of the platens is the same as that of the specimen (within $\pm$0.05 mm),

(3) Two diametrically positioned linear variable differential transformers (LVDT) clamped on the top and bottom platens to measure axial displacements,

(4) A load cell located underneath the bottom platen.

Long term stability of the cell and pore pressure systems is assured with computer-controlled stepping motor pumps equipped with an uninterruptable power supply. Cell and pore pressure can be maintained within $\pm$5 kPa of the target pressure over a period of a few months. With tests spanning extensive time periods on individual samples (9 months for the results presented here), changes in temperature can be significant and may have a considerable effect on the test results, particularly on pore pressure measurements. The cell and the loading frame are well insulated and the temperature control system is capable of maintaining a constant temperature within $\pm$0.5°C over a period of a few months. No diurnal pore pressure fluctuations were noted. The tests reported here were performed at room temperature.

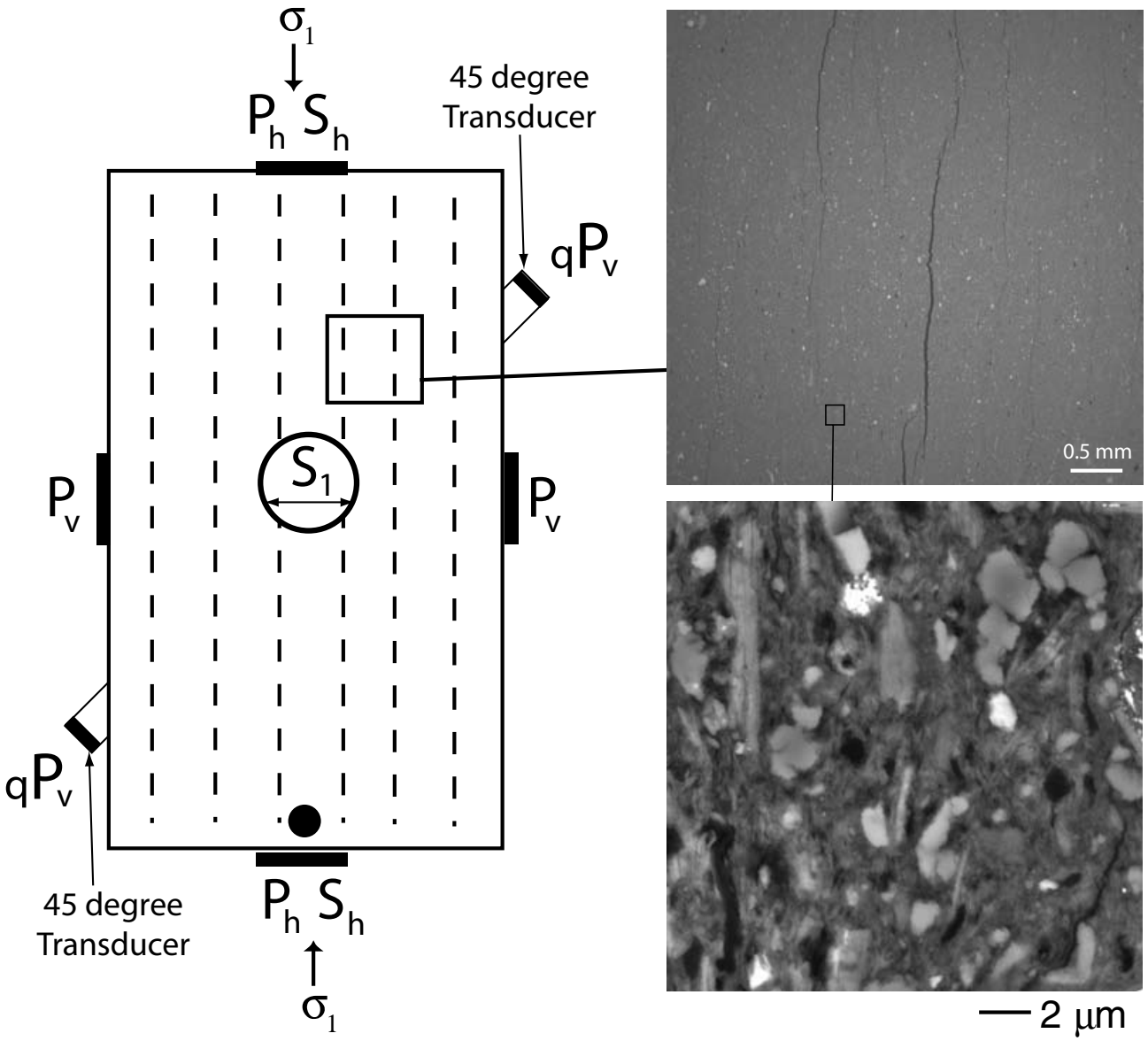

Figure 1. Experimental configuration of the single core plug method for assessing ultrasonic anisotropy. The orientations of the various velocities with respect to the fabric elements are shown. Both particle alignment and microcracks are parallel to the core axis and hence the direction of maximum applied stress. The *P*-wave transducers at 45° to the core axis are shown in black, located at the ends of acrylic resin wedges and are diametrically opposed to one another.

Typically, measurements for velocity anisotropy in shales required the use of multiple core plugs thus further increasing time required for such tests to be performed. However, Wang (2002b) overcame some of these problems by devising an ultrasonic configuration where measurements could be made on a single core plug and reported a series of results for a suite of common sedimentary rocks including shales (Wang 2002a), most of which were shown to be highly anisotropic. In a similar fashion, we designed and have used for several years an experimental configuration (Fig. 1) that allows the full elastic tensor to be calculated from a single core assuming that the shale is a TI medium. *P*-wave and *S*-wave velocities can be measured through the end platens that house 1 MHz, PZT-5H piezo-ceramic *P*-wave and *S*-wave elements to measure velocity down the core axis. In addition, orthogonal *P*- and *S*-wave transducers are located on the membrane for measurements of velocity across the core diameter. A post on the aluminium shear-wave transducer housing penetrates through the Viton membrane to rest against the sample and improves identification of *S*-wave arrivals (Fig. 2), sometimes a major difficulty in shales. Also, a pair of *P*-wave elements (set in cylindrical wedges of acrylic resin and directly facing one another) transmits and receives pulses at 45° to the core axis. This configuration of wedges was necessary in order to make all necessary measurements for the determination of the stiffness tensor on a single core with the shale principal axes aligned with the cell rather than using a number of cores cut at varying angles to the principal axes (e.g. Dellinger & Vernik 1994; Hornby 1998). Calibrations of the array were performed using aluminium, acrylic resin and phenolite cylinders of similar geometry to

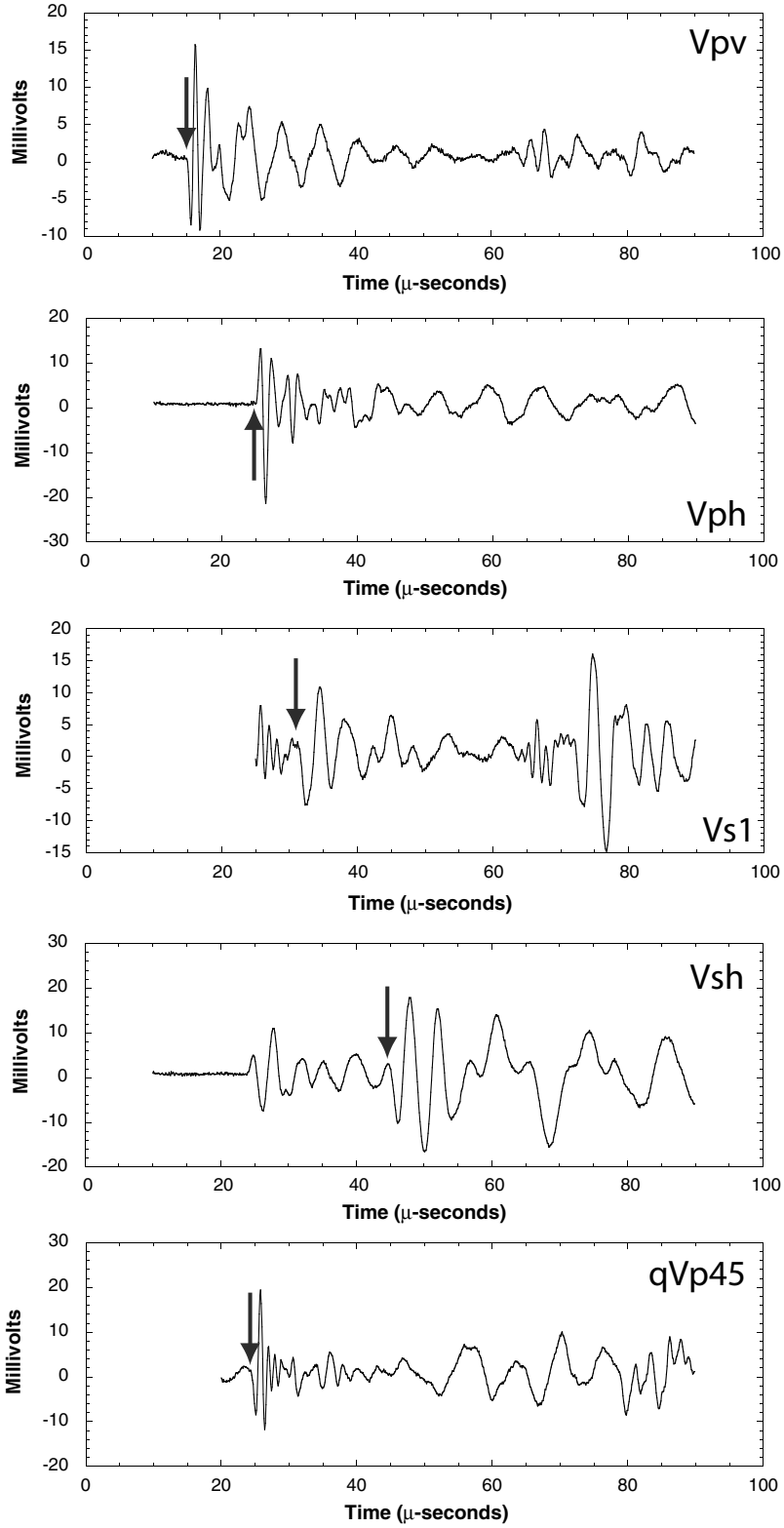

Figure 2. Examples of waveforms taken during the experimental cycle on Muderong Shale at ~40 MPa mean effective stress. *S* waves are usually hard to pick in shales, but using a new methodology (see text), waveforms and hence picks were much more certain.

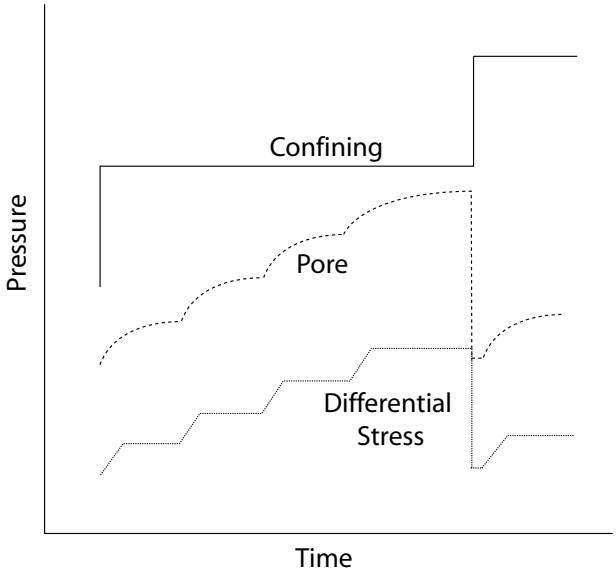

Figure 3. Details of the stress path used in these tests. Confining pressure is raised to a set level, whereupon a differential stress is applied in increments in an undrained state until within ∼10 per cent of peak strength. At this point, differential stress is reduced, pore pressure drains to back pressure and confining pressure is increased and the cycle starts over again.

the test samples. Ultrasonic parameters measured during the shale triaxial testing programme included P_V, P_H, S_1, S_H and quasi-P (qV_{p45}) at nominal centre frequencies of 0.6–1.0 MHz (for *P* waves) to 0.2–0.4 MHz (for *S* waves). Examples of waveforms are shown in Fig. 2. Arrival time picks were based on first breaks estimated from approximately 1 per cent of the first peak amplitude. Uncertainties were ± 0.1 μ seconds for *P*-wave arrival times and ± 0.2 μ seconds for *S* waves, corresponding to velocity errors of ± 0.4 per cent. Picking errors are reduced as effective stress increases, especially for *S* waves. Errors in elastic constants are generally <1 per cent, with the exception of c_{13} where errors are estimated as ∼2 per cent, while errors in the anisotropy parameters are higher due to the use of ratios of elastic constants. Here, errors in ε and γ may range up to 2 per cent, while δ has the least accuracy, with errors of typically ± 13 per cent.

For the geomechanical tests, initial confining and pore pressures were 10 MPa and 5 MPa, respectively, under drained conditions. Pore pressure control is critical as gas will exsolve from solution during core recovery, rendering shales partially saturated. A pore pressure of 5 MPa ensures the shale will become fully saturated at the start of the experimental process. This has been a problem with many previously published shale tests where samples were tested 'dry', unsaturated or partially saturated when drained to atmosphere. Differential stress was applied stepwise in the undrained condition (Fig. 3) until within ∼10 per cent of peak stress at failure (previously determined by Dewhurst & Hennig 2003). Ultrasonic recordings were made when pore pressures reached constant values and axial deformation had stabilized (Fig. 3). This could take a few days to several weeks. Once these conditions were established, the next increment in axial load was applied. After reaching the maximum differential stress at a given confining pressure, differential stress was reduced to ∼0.5 MPa (to keep the ram in contact with the sample train) by decreasing axial load, pore pressure allowed to drain to 5 MPa and confining pressure was increased to the next level under drained conditions. The results reported here were performed using a multistage consolidated undrained test (Fjær *et al.* 1992) on a single core plug. Confining pressures used were 10, 15, 25, 45 and 65 MPa.

THE MUDERONG SHALE

The fine-grained nature of shales and their characteristic physico and electrochemistry necessitates the use of special techniques to ensure that samples are tested in as close to a representative state as possible. This requires therefore that precautions are taken to avoid desiccation of shales after coring to avoid fracturing of the shale, inducing large capillary stresses (possibly in excess of 5 MPa, e.g. Horsrud *et al.* 1998) and changes of particle orientation and pore size distribution. The Muderong Shale used in these tests comes from a 4 m core recovered from a well in the offshore northern Carnarvon Basin on the Northwest Shelf of Australia from a depth of ∼1120 m. It was sealed in wax after recovery and shipped to land. Sub-samples for geomechanical testing, cylinders of 76 mm length and 38 mm diameter, were taken immediately and stored under light process oil to prevent evaporation of pore fluids. Offcuts from these samples were used for sample characterization in terms of grain size distribution, pore size distribution, porosity, specific surface area, composition, grain density and microstructural evaluation. These samples were similarly stored until tested.

Other problems often encountered with shales are a result of their low permeability and physicochemistry (Horsrud *et al.* 1998). Clay minerals have a characteristic surface charge and high specific surface area that renders them susceptible to reaction with contacting pore fluids. As such, care was taken to determine the pore fluid composition in the Muderong Shale samples recovered and a synthetic pore fluid based on this composition was manufactured and used in the geomechanical experiments. Sample swelling could be monitored within the triaxial configuration, but no reaction was noted between the pore fluid used and the Muderong Shale cores.

Co-dominant minerals in the Muderong Shale are mixed layer illite-smectite (∼60 per cent illite layers) and quartz (∼30 per cent each) with lesser amounts of kaolinite, discrete illite and chlorite.

Clay fraction is ∼40 per cent, clay content ∼65 per cent. Porosity is ∼17 per cent, bulk density is 2.20 g cm^{-3}, permeability is <1 nD (Bernhard Krooss, personal communication, 2004), modal pore throat size is ∼25 nm, cation exchange capacity is ∼15 meq/100 g and specific surface area by nitrogen adsorption is ∼30 m^2 g^{-1} (Dewhurst *et al.* 2002a; Dewhurst & Hennig 2003). Under the scanning electron microscope (Fig. 1), the Muderong Shale is a non-laminated shale with clay matrix support, with a preferential particle orientation and, at ambient pressures, contains high aspect ratio microfractures parallel to the compaction fabric of the shale, which have resulted from stress relief during coring, not desiccation (see Dewhurst *et al.* 2002a; Dewhurst & Hennig 2003, for justification). Preferential particle orientation of both rigid grains and clay matrix can be observed, although the clay matrix orientation can be affected locally by the presence of more rigid particles. Fabrics such as these are the primary control on the TI nature of shales. Fuller details of composition, properties and microstructure of Muderong Shale can be found in Dewhurst *et al.* (2002a) and Dewhurst & Hennig (2003). The orientations of the structural and sedimentary anisotropies in relation to the ultrasonic measurements are shown in Fig. 1.

GROUP OR PHASE VELOCITY?

The most error prone of the ultrasonic measurements is that of the off-axis measurement of the quasi *P*-wave or *S*-wave velocities. There has been considerable debate in the literature concerning whether experimental velocities measured in the laboratory are phase or group velocities (e.g. Hornby 1998; Dellinger & Vernik 1994). These latter authors used cores cut at 45° to bedding with transducers attached to the core ends and concluded that they were measuring phase velocities. In the experiments described in this paper, measuring the full elastic tensor on a single core plug, we used cylindrical acrylic resin wedges for the off-axis transducers with the wedge velocity matched to the slow *P*-wave velocity (V_{pv}) in the shale. In order to clarify the interpretation of the observed velocities we have carried out numerical solutions for the propagating wave fronts using an anisotropic finite difference code (Wang 2001). Wavefield snapshots are shown in Figs 4(a)–(c). It should be noted that as the transducers are housed at the end of the acrylic wedges, wave propagation starts in the acrylic wedge which is a short distance from the surface of the shale core plug. The model results show that the normal to the first arrival meets the receiving transducer at an angle θ, which is somewhat less than 45° to the principal axis. In general, all arrivals observed in anisotropic media are group arrivals other than those travelling along principal axes where group velocities are equal to phase velocities. Since determination of c_{13} requires knowledge of the phase velocity, $qV_{p\theta}$, it is necessary to solve for the eigenvalues of the Christoffel equations (Helbig & Schoenberg 1987; Tsvankin 2001). Eigensolutions to the Christoffel equation for VTI materials are given by:

$$\begin{vmatrix} c_{11}\sin^2\theta + c_{44}\cos^2\theta - \rho V_{\text{phase}}^2 & (c_{13}+c_{44})\cos\theta\sin\theta \\ (c_{13}+c_{44})\cos\theta\sin\theta & c_{44}\sin^2\theta + c_{33}\cos^2\theta - \rho V_{\text{phase}}^2 \end{vmatrix} = 0, \quad (14)$$

where θ is the angle of the wave front normal with respect to the symmetry axis and V_{phase} is the phase velocity. At oblique angles the waves are termed *quasi-P* waves. Eq. (14) is also quadratic in c_{13} giving two means of calculating c_{13}, either via the *P*-wave phase velocity or the *S*-wave phase velocity.

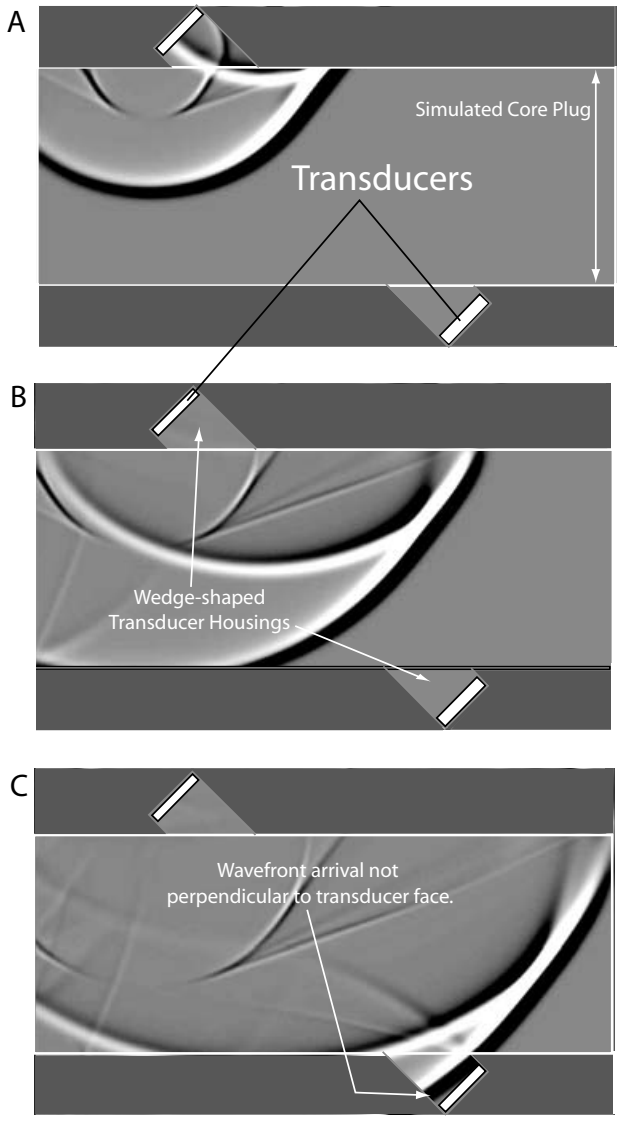

Figure 4. Synthetic wavefield snapshots of off-axis pulse propagation through a shale core at (a) 8 μs, (b) 14 μs and (c) 20 μs. Transducers are shown as white blocks housed at the end of acrylic wedges, facing one another. Note that the arrival at the lower transducer (c) shows that propagation is not normal to the wave front and as such represents a group velocity.

The group velocity is given by Tsvankin (2001) as:

$$V_{gx} = V_{\text{phase}}\sin\theta + \frac{\partial V_{\text{phase}}}{\partial\theta}\cos\theta$$
$$V_{gz} = V_{\text{phase}}\cos\theta - \frac{\partial V_{\text{phase}}}{\partial\theta}c\sin\theta \quad (15)$$

where V_{gx} and V_{gz} are the x and z components of the group velocity vector, respectively.

From eqs (14) and (15), c_{13} can then be calculated by solving simultaneously for θ and V_p using an observed group velocity at a ray path angle, ϕ, of 45°. A non-linear simultaneous equation solver was used to give θ, V_p and ultimately c_{13}, at each stress condition. Our method of calculating c_{13} is as follows:

(1) Determine c_{11}, c_{33} and c_{55} from arrival times (and subsequently velocities with appropriate propagation modes and polarizations) along principal axes.

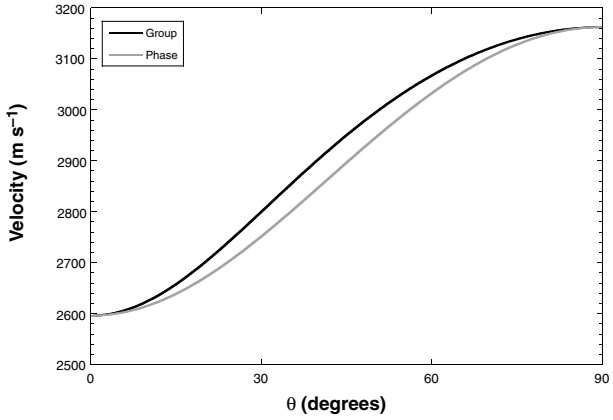

Figure 5. Group and phase velocity surfaces for the Muderong Shale at one effective stress condition.

(2) Determine the magnitude of the quasi *P*-wave group velocity from the arrival time and the known ray path (the distance between centres of the transmitter and receiver transducers in Figs 1 and 4).

(3) Solve for c_{13} by treating θ and V_{phase} as parametric or common variables and solving the combination of eqs (14) and (15) simultaneously such that $V_{gx}/V_{gz} = 1$ ($\phi = 45^\circ$ ray) and $\sqrt{V_{gx}^2 + V_{gz}^2}$ is equal to the experimental group velocity. We can also calculate θ and V_{phase} that meets those conditions if required.

For example, from our experiments a typical experimental set of density-normalized shale elastic stiffnesses are $c_{11} = 10.0$ (km s^{-1})$^{-2}$, $c_{33} = 6.74$ (km s^{-1})$^{-2}$ and $c_{44} = 1.46$ (km s^{-1})$^{-2}$. The experimental *quasi P-wave* group velocity at 45° to the principal axes is 2841 m s^{-1}. This yields a c_{13} value of 5.29 (km s^{-1})$^{-2}$. The corresponding phase velocity is 2788 m s^{-1} at an angle, θ, of 33.93°. The velocity surfaces derived from these stiffness parameters are shown in Fig. 5. However, had we assumed that the measured velocity of 2841 m s^{-1} was a phase velocity at 45° to the principal axes then a c_{13} value of 4.638 (km s^{-1})$^{-2}$ would be obtained, an error of −12.4 per cent.

Our conclusion of group versus phase differs to those of Hornby (1998), Sayers & Ebrom (1997) and Dellinger & Vernik (1994) due to the different configurations of the experiments we used (i.e. full elastic tensor measurements on a single core plug). The quoted authors made measurements on core plugs cut in different orientations relative to bedding with transducers directly in contact with those core plugs.

RESULTS

A nett pressure–velocity plot for Muderong Shale is shown in Fig. 6(a) and shows that the velocity response to nett pressure change is not a simple monotonic function, as the effect of axial loading is ignored. The only stress that the dynamic elastic properties of this shale responded to in an almost monotonic manner was the mean effective stress (see eq. 4 above). The influence of mean effective stress on the ultrasonic velocity in Muderong Shale can be seen in Fig. 6(b). V_{pv} increases from ∼2380 to ∼2800 m s^{-1} as mean effective stress increases from 5 to 60 MPa, while V_{ph} rises from ∼2890 to ∼3380 m s^{-1} over the same stress range. V_{s1} increases from ∼1130 m s^{-1} to ∼1380 m s^{-1} while V_{sh} rises from 1650 to 1940 m s^{-1} as mean effective stress increases from 5–60 MPa. The quasi-*P* velocity increases from ∼2550 to ∼3200 m s^{-1} over the same stress range and lies between V_{ph} and V_{pv}. This shale therefore shows a high degree of anisotropy in velocity. Additionally, the velocity-mean effective stress curves are almost linear, with only very slight deviations from linearity at low effective stress levels.

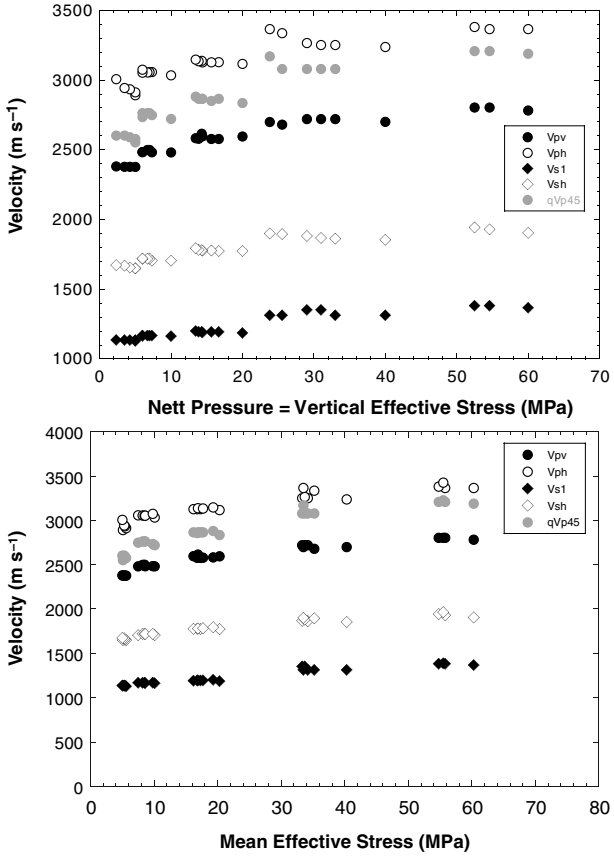

Figure 6. (a) Nett pressure–velocity plot for Muderong Shale and (b) Mean effective stress-velocity plot for Muderong Shale. A smooth relationship is only evident for velocity increasing with mean effective stress. Note significant anisotropy in velocity, linearity of the response at low stress and the non-symmetrical response of qV_{p45}.

V_{pv}/V_{s1} ratios are relatively invariant but do increase slightly with increasing mean effective stress (from 2.09 to 2.19, Fig. 7a) up to 20 MPa, after which they decrease to ∼2 at the highest effective stresses. Dynamic Poisson's ratios calculated from these ratios (∼0.34–0.37) are unusually consistent with static values (∼0.35–0.40) measured previously by Dewhurst & Hennig (2003) from axial and radial strains derived during standard triaxial tests. The ratio V_{ph}/V_{sh} is also relatively insensitive to stress increase, decreasing from 1.80 to 1.74 over the 5–60 MPa stress range used in these tests (Fig. 7a). As a comparison, an isotropic compaction test on fully saturated Pierre Shale (again a smectite-rich shale) also shows increasing V_{pv}/V_{s1} ratio with increasing stress at low stress levels (Fig. 7b).

The response of the elastic coefficients, c_{11}, c_{33}, c_{44}, c_{66}, c_{12} and c_{13}, are shown in Fig. 8. All increase monotonically as mean effective stress increases by between 33 and 114 per cent. c_{11} increases from ∼20 GPa to ∼27 GPa, while c_{33} rises from ∼13 to 18 GPa as mean effective stress increases from 5 to 60 MPa. c_{44} and c_{66} increase from ∼3 to 4.5 and ∼6 to 9 Gpa, respectively, over the same stress range. c_{12} rises from ∼6.8 to 9.5 GPa but c_{13} shows the most stress

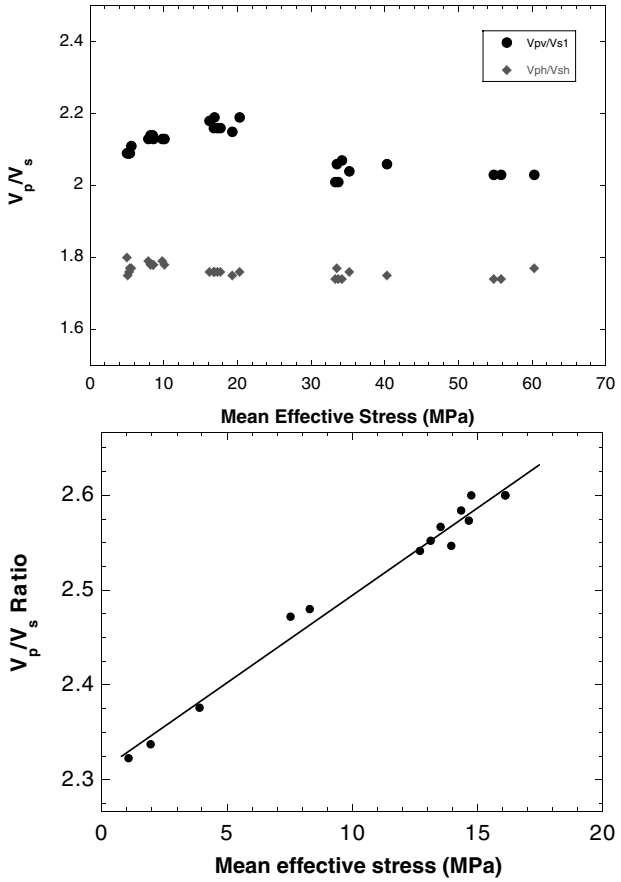

Figure 7. Influence of mean effective stress on V_p/V_s ratios in both Muderong Shale (a) and Pierre Shale (b). V_p/V_s ratios increase as stress increases in fully saturated shales.

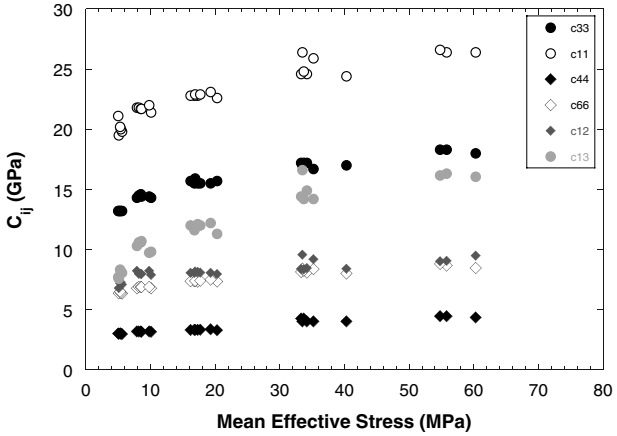

Figure 8. Mean effective stress-c_{ij} plot for Muderong Shale. Note significant anisotropy, linearity of the response at low stress and that c_{13} appears to be the most sensitive parameter to changing stress.

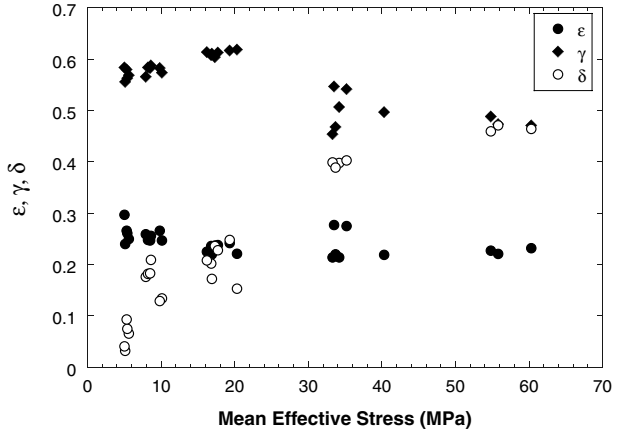

Figure 9. *P*- (ε) and *S*-wave (γ) anisotropy factors both decrease with increasing mean effective stress. The wave front anellipticity factor (δ) increases as stress increases.

sensitivity, increasing from 7.6 to 16.2 GPa as mean effective stress rises to 60 MPa.

The elastic coefficients calculated above are used to derive the anisotropy parameters defined in eqs 11–13 above (from Thomsen 1986). The influence of mean effective stress on *P*-wave (ε) and *S*-wave (γ) anisotropy factors as well as the wave front anellipticity factor (δ) is shown in Fig. 9. Initial anisotropy at low stress is seen to be large (0.3 for *P* waves, 0.6 for *S*-waves) and variable with changing mean effective stress. ε decreases from ∼0.30 to 0.21 as mean effective stress increases from 5 to 60 MPa. γ initially is ∼0.6, but at stresses >20 MPa it begins to decrease, reaching ∼0.47 and at 60 MPa. δ increases from 0.04 to 0.47 as mean effective stress increases from 5 to 60 MPa.

In addition, part of the rationale behind these tests was to evaluate the influence of differential stress (as defined above in eq. 3) on ultrasonic properties. The influence of differential stress (or stress anisotropy) can be assessed from plots of nett pressure (as defined in eq. 1 above) against velocity. *P*-wave velocity (V_{pv}) is seen to increase by up to ∼100 m s^{-1} at any given nett pressure as differential stress increases from a state of almost isotropic stress (differential stress of 0.46 MPa) to ∼8 MPa (Fig. 10a). Variations in V_{s1} at any given nett pressure range between ∼20–100 m s^{-1} as differential stress increases to 8 MPa (Fig. 10b). However, in terms of anisotropy, ε is seen to be relatively independent of differential stress, generally varying by <0.02 at any given nett pressure (Fig. 11a). Although there is more scatter when γ is examined (Fig. 11b), again it seems likely that it is generally unaffected by increasing differential stress. However, δ does appear to be affected by increasing differential stress, showing a maximum increase of ∼0.15 (from 0.25 to 0.40) at nett pressures of ∼30 MPa (Fig. 11c). While such a difference is outside the level of experimental error estimated for δ (typically 13 per cent, see above), there are only a few data points on which this observation is based, so the results should be treated with caution.

Further to these tests outlined above, another test was run on Muderong Shale under isotropic stress conditions to ∼12 MPa effective stress (Fig. 12). While this stress range was considerably smaller than that investigated in the previous tests, the velocity and c_{ij} magnitudes are consistent with the low stress end of those tests. However, the significant differences between this isotropic test and the other tests conducted under an anisotropic stress field, are that γ drops from ∼0.6 to ∼0.25 when mean effective stress exceeds 5 MPa and that δ is negative and decreases with increasing stress (*cf.* Figs 9 and 12).

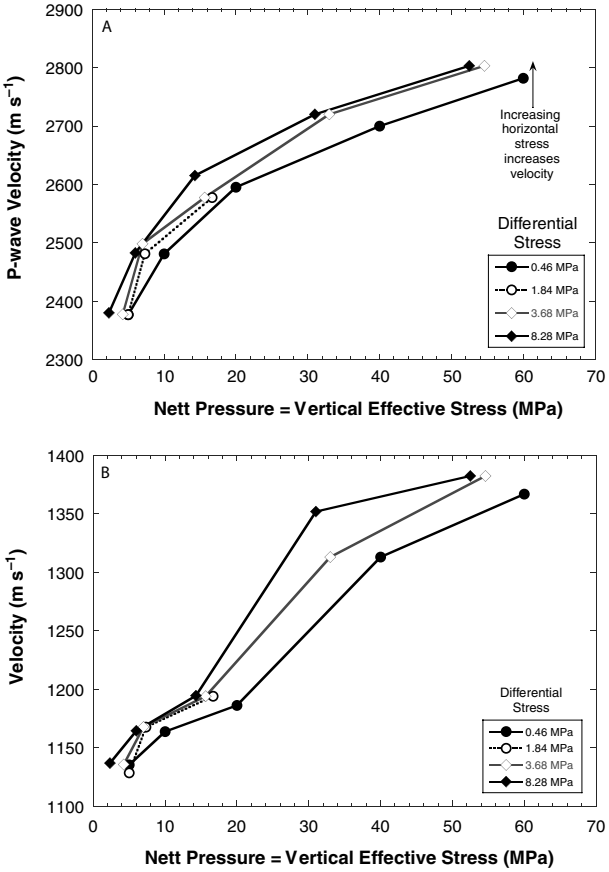

Figure 10. (a) *P*-wave and (b) *S*-wave velocity both increase as differential stress increases at any given nett pressure.

DISCUSSION

The results presented above raise a number of issues with regard to shale response to the passage of ultrasonic waves. Velocities and c_{ij}'s increase with increasing mean effective stress and show linear behaviour at low stress, plus c_{13} is the most stress sensitive elastic coefficient. V_p/V_s ratios and hence dynamic Poisson's ratios either increase or remain almost constant with increasing mean effective stress, which is somewhat counter-intuitive compared to most documented rock responses. This shale is also highly anisotropic with its anisotropy factors sensitive to stress to different degrees. Furthermore, increasing stress anisotropy causes changes in velocity and δ but ε and γ are relatively unchanged.

Effect of Stress Increase

The increases in both velocity and elastic coefficients (Figs 6 and 8) with increasing mean effective stress are usually ascribed to porosity loss, grain contact stiffening and microcrack closure, while non-linear behaviour at low stress is often related to cracks closing. While porosity was not explicitly measured in these tests, the total axial strain measured up to 60 MPa mean effective stress in these tests was ∼1 per cent, indicative of little porosity loss from the initial value of 17 per cent. Previous tests have shown that it is difficult to mechanically compact a shale with small pores (modal pore throat size of ∼20 nm in this case; Dewhurst *et al.* 2002a) in the laboratory to below 20 per cent porosity even at high stress levels (e.g. Dewhurst *et al.* 1998). Hence, porosity loss is not likely to be a factor in this case.

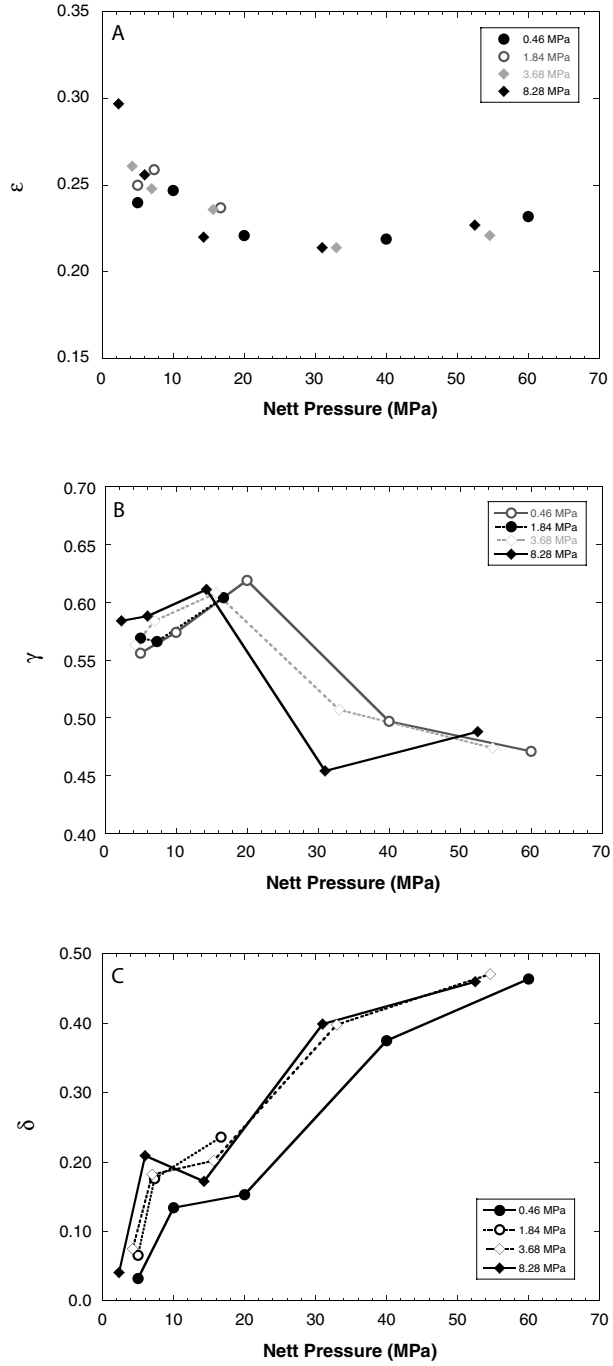

Figure 11. Increasing differential stress at constant nett pressure seemingly has little effect on ε (a) or γ (b), but may affect δ (c) to a larger extent.

Non-linearity of velocity-effective stress curves at low effective stresses has been documented in a number of rock types, including granites, sandstones and shales. Such non-linearity has usually been ascribed to the closure of microcracks at grain boundaries. However, not all shales are documented to behave in this fashion. Johnston (1987) documents curvature of the velocity-effective stress relationship at low stress in pore pressure controlled tests, but indicates that

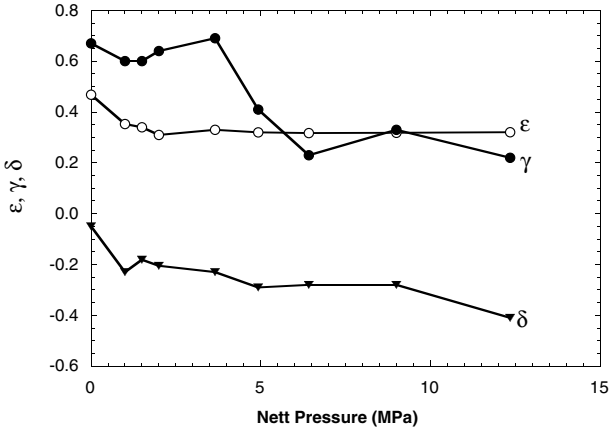

Figure 12. Change in anisotropy factors with increasing stress under isotropic conditions in a low stress experiment on Muderong Shale.

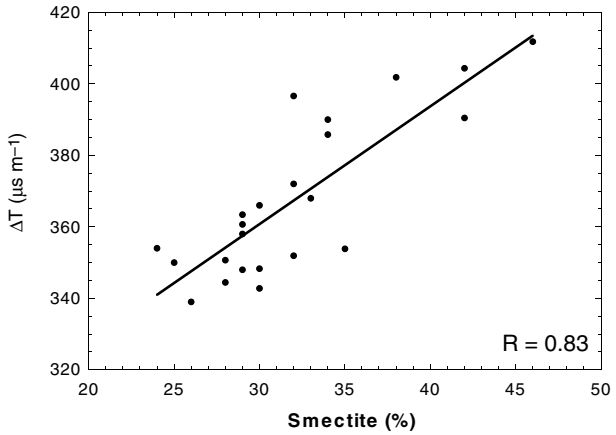

Figure 13. Influence of mixed layer illite-smectite on *P*-wave transit time (reciprocal of velocity) in wireline logs from the Muderong Shale at approximately constant (vertical) effective stress of 25–30 MPa.

in the shales he tested, such non-linearity was far smaller than that seen in sandstones. Hornby (1998) does observe non-linearity in shales at low effective stress in saturated samples. Jones & Wang (1981) document non-linear behaviour at low stress in a shallow, less compacted shale but more linear behaviour in more deeply buried lithified shale. Non-linear behaviour in shales was also noted by Johnston & Christensen (1995) as well as Vernik & Landis (1996) but these tests were conducted under unsaturated and 'dry' conditions, respectively. One of the problems with comparing the results for shales that are available is that few of the previous tests were performed with pore pressure control on well-preserved samples. Some tests are described as 'dry', some unsaturated and some saturated, but even the latter are unlikely to be fully saturated without pore pressure control and even a small departure (<1 per cent) from full saturation can significantly influence ultrasonic properties (e.g. Mavko & Mukerji 1998). In one of the few sets of tests performed under controlled pore pressure (and, therefore, fully saturated) conditions, Domnesteanu *et al.* (2002) note non-linear velocity-effective stress relationships at low stress in a quite coarse-grained and permeable (20 μD) shale. Jakobsen & Johansen (2000) note apparent non-linear behaviour in *P* waves at low stresses, but linear behaviour for *S* waves in pore pressure controlled tests. However, their loading cycle changed from isotropic to axial during the experiment and analysis of the isotropic part alone suggests an almost linear velocity-effective stress relationship.

The low stress velocity response of the Muderong Shale is almost linear (Fig. 6). Bedding parallel microfractures have been documented in the shale we tested (Fig. 1) and such fractures in these tests were aligned parallel to the maximum principal stress, the ideal orientation for opening. Hence, increasing mean effective stress, through increasing axial load, is likely to result in bedding-parallel fractures remaining open as stress increases, thus accounting for the linear response observed at low effective stress. In addition, previous tests run dry or without pore pressure control allow freer fluid movement from high aspect ratio cracks as they close with increasing stress. Our tests were run in an undrained state and the matrix permeability of Muderong Shale is <1 nD, thus restricting fluid egress from open fractures. In such a scenario, fractures may exhibit decreased compliance or at the very least, time-dependent compliance changes as a result of the low permeability, undrained conditions. Hence, pore pressure control in shale tests is a critical issue with regard to full saturation of pores and fractures, due to the effects of saturation on crack compliance and concomitant ultrasonic response.

A further issue to note here is that in absolute terms, *P*-wave velocity increases more with increasing stress than *S*-wave velocity in Muderong Shale (Fig. 6). This sort of behaviour has also been noted in a number of shales in the literature (e.g. Johnston 1987; Holt *et al.* 1991). In fact, *S* waves travelling through Muderong Shale, Pierre Shale and a number of smectite-rich shales in the literature, are relatively insensitive to effective stress change below about 25 MPa. An extreme example of this is Fuller's earth, a bentonite tested by Holt *et al.* (1991), where both *P*- and *S*-wave velocity were almost totally insensitive to effective stress change to 22 MPa. The presence of smectite in the Muderong Shale has been noted to influence wireline log *P*-wave velocity (Fig. 13; see also Dewhurst *et al.* 2002b). This is likely due to the presence of bound interlayer water within the mineral structure which reduces bulk density and would likely affect *S*-wave velocity where propagation is normal to the mineral structure and polarization is parallel. In the Muderong Shale, *S*-wave velocity increases slightly up to 20 MPa effective stress. However a jump in velocity is seen between 20 and 40 MPa, which may be associated with the loss of interlayer water from the mineral structure. Stress increases have previously been associated with interlayer water loss from smectites (Fitts & Brown 1999; Lal 1999). The latter author notes loss of interlayer water at stresses exceeding 27 MPa, consistent with stress levels where *S*-wave velocity is observed to increase in Muderong Shale. Given the little porosity change noted during these experiments, it is likely that grain contact stiffening and also stiffening of the smectite crystal structure due to loss of interlayer water are responsible for the velocity increases seen in the Muderong Shale.

Regarding the elastic coefficients (c_{ij}'s), while the principal coefficients parallel to the core axis and symmetry axis behave in a similar way to velocity (i.e. they show an almost linear behaviour at low stress levels and increase with increasing mean effective stress), it is noted that c_{13} appears to be the most sensitive coefficient to stress change (Fig. 8). The likely explanation for this result is most easily explained in terms of compliance (S_{13}), as this can be viewed as a direct coupling of stress parallel to the symmetry axis and strain in the plane of symmetry (e.g. Lekhnitskii 1981), such that:

$$S_{13} = \frac{-\nu}{E_z} = \frac{\varepsilon_r}{\sigma_z}, \tag{16}$$

where ν is Poisson's ratio, E_z is Young's Modulus parallel to the symmetry axis, ε_r is strain in the plane of symmetry and σ_z is stress applied parallel to the symmetry axis (or normal to the plane of symmetry), which in our tests is σ_3 (the confining pressure, Fig. 1). As c_{13} (a stiffness coefficient) increases with increasing stress (Fig. 8), it follows that compliance decreases as mean effective stress rises. Decreasing compliance with rising stress can be attributed to two factors in these experiments:

(1) From eq. (16), σ_z in our experiments is the confining pressure. Changes in confining pressure cause isotropic compaction and as such, serve to close fractures and increase grain contact stresses, thus decreasing compliance. This is also consistent with decreasing anisotropy as mean effective stress increases since nett pressure (eq. 1) has more effect on anisotropy than differential stress (eq. 3, Fig. 11).

(2) Our experiments were conducted in the undrained state in a low-permeability (<1 nD) medium. Cracks in this shale (Fig. 1) are fluid filled, isolated and discontinuous (Dewhurst *et al.* 2002a). The low-permeability matrix results in increasing pore pressure as loading occurs and also would prevent rapid fluid escape (e.g. squirt flow) from cracks during the propagation of an ultrasonic wave. This would have the effect of further reducing overall compliance (see also Domnesteanu *et al.* 2002).

While shales are generally considered TI media, the alignment of the maximum principal stress normal to the TI axis of symmetry in these tests might mean that the TI assumption could be considered dubious. However, the fact that *P*- and *S*-wave anisotropy remain relatively constant as differential stress increases at any given level of nett pressure (Fig. 11) tends to suggest that the impact of differential stress change on anisotropy is minimal and thus the TI assumption would appear to hold in this case. However, it should be borne in mind that the Muderong Shale used in these tests is weak and the differential stress levels shown in Fig. 11 are quite low (up to ∼8 MPa only). In stronger rocks where higher differential stresses are attained, the TI assumption may not still be valid where the maximum stress direction is oriented normal to the TI symmetry axis.

V_p/V_s ratios

In part, the tests outlined above showed some counter-intuitive behaviour in that up to ∼20 MPa mean effective stress, V_p/V_s ratios increase with increasing stress. This behaviour is observed in both Muderong Shale and Pierre Shale (at low stress) under fully saturated conditions (Fig. 7). Generally, it would be expected that V_p/V_s ratios (and dynamic Poisson's ratio) would decline as stress increased in a saturated rock (e.g. Siggins & Dewhurst 2003). A review of the literature indicates that both increases and decreases in Poisson's ratio in shales have been observed with stress increase but such a picture is again further complicated by lack of pore pressure control in most experiments on shales to date. In isotropic compression tests, Johnston & Christensen (1994, 1995) note that V_p/V_s ratios increase with stress up to 200 MPa in tests on unsaturated samples with no pore pressure control. Hornby (1998) showed that V_p/V_s ratio decreased with increasing stress in an illite/kaolinite-rich shale but remained almost constant (decreased from 1.90 to 1.86) in a shale containing smectite with increasing isotropic stress to 80 MPa in tests drained to the atmosphere. Johnston (1987) observed slightly increasing dynamic Poisson's ratio (and therefore V_p/V_s ratio) with increasing stress in two shales, one containing dominantly quartz and mixed layer illite-smectite, the other quartz and discrete illite. These tests had in situ equivalent pore pressures. Also pore pressure controlled were tests by Domnesteanu *et al.* (2002), who noted that V_p/V_s ratios decreased with increasing isotropic stress in a coarse-grained (20–80 μm), relatively permeable (20 μD) shale with a high proportion (59 per cent) of coarser-grained quartz and feldspar particles and minimal (6 per cent) mixed layer illite-smectite. Jones & Wang (1981) noted increasing V_p/V_s ratios with increasing isotropic stress in tests without pore pressure control and in shales containing ∼10 per cent each of smectite and illite. Holt *et al.* (1991) also note increasing V_p/V_s ratio in Weald Shale with stress increase (to ∼10 MPa effective stress) and pore pressure control (at 2 MPa), while it is unchanged in Fuller's earth as velocity in this clay is completely stress insensitive (to ∼22 MPa effective stress). In a series of tests on chlorite, illite and kaolinite-rich shales, Jakobsen & Johansen (2000) also noted constant or slightly increasing V_p/V_s ratios with increasing mean effective stress to ∼15 MPa with pore pressures of 1 MPa.

One of the problems with determining the mechanism of V_p/V_s ratio increase is that most of the documented tests in the literature have been performed under non-standard conditions, in that samples have been unsaturated or partly saturated with no pore pressure control. In addition, it is likely that composition, especially the presence of mixed layer illite-smectite, has a significant influence on ultrasonic response (e.g. Vernik & Liu 1997). Increasing V_p/V_s ratios with increased stress would be consistent with conditions of partial saturation in shales (e.g. Sayers *et al.* 2001, their Fig. 5). In our tests, increased V_p/V_s ratios were noted in fully saturated Pierre Shale (Skempton's B coefficient of 0.998; Skempton 1954), and fully saturated Muderong Shale to 20 MPa mean effective stress (this shale was too lithified for a Skempton B test, but had pore pressure of 5 MPa or more during the whole 9 months of testing). Both of these shales are rich in mixed layer illite-smectite. The two shale tests of Johnston (1987) also had pore pressure control and show slightly increasing dynamic Poisson's ratios with stress; of these, one shale was rich (∼25 per cent) in mixed layer illite-smectite, while the other had small amounts (∼5 per cent). The shale of Domnesteanu *et al.* (2002) did have pore pressure control but comprises ∼60 per cent rigid, non-clay particles with modal pore throat size of 30 μm (*cf.* Muderong Shale ∼20 nm), suggesting a rigid particle framework; such a particle arrangement typically results in V_p/V_s ratios decreasing with increasing stress as typically seen in sandstones and siltstones. The Muderong Shale contains ∼65 per cent clay which forms the grain framework and ∼35 per cent of the shale is mixed layer illite-smectite (Dewhurst *et al.* 2002a). Given that *P* waves are generally less affected by liquid-filled cracks (in this case the smectite interlayer water) but that *S* waves show a significant reduction in velocity in such a scenario, it is likely that *S*-wave propagation normal to the strong compaction fabric in Muderong Shale will have both polarization directions oriented parallel to the hydrated interlayers, which will result in low *S*-wave velocity and increasing V_p/V_s ratios with stress increases. Larger increases in *S*-wave velocity are noted above 20 MPa mean effective stress resulting in slightly decreasing V_p/V_s ratios and as noted above, this is likely due to stress-induced loss of interlayer water (Lal 1999) stiffening the smectite mineral structure.

Elastic anisotropy

Velocity anisotropy in the Muderong Shale is high, with Thomsen's parameters ε and γ being ∼0.3 and 0.6, respectively, under low stress conditions. The high values of ultrasonic anisotropy seen in the

Muderong Shale are consistent with a few other smectite-rich hard shales reported in the literature (e.g. Thomsen 1986; Hornby 1998; Wang 2002a). The latter author notes that ultrasonic anisotropy in shale depends on porosity, compaction history and clay composition. Changes in anisotropy under isotropic stress conditions have been ascribed to changing particle alignment and decreasing porosity (Hornby 1998). The Muderong Shale is a stiff shale with a pre-existing strong particle alignment and a high mixed layer illite-smectite content. Porosity changed little during the experiment and particle re-orientation is unlikely in a compacted shale. Hence other mechanisms need to be found to explain changes in anisotropy with increasing stress in the Muderong Shale. It is likely that all laboratory-tested shale samples contain stress relief microfractures, which will significantly increase anisotropy. Holt *et al.* (2004) noted that V_{pv} was more sensitive than V_{ph} at low stress in shales and suggest that this is indicative of core damage. However, while there is evidence for the presence of stress relief cracks in the Muderong Shale (Fig. 1), the velocity response is linear at low stress for both V_{pv} and V_{ph}, indicating that the observation of Holt *et al.* (2004) may not always be diagnostic for shales.

In its initial state, the Muderong Shale has a strong compaction fabric of aligned clay particles and fluid-filled microcracks parallel to the compaction fabric (Fig. 1), which commonly cause ultrasonic anisotropy. Low *S*-wave velocity (V_{s1}) resulting from the presence of mixed layer illite-smectite also likely contributes to the extreme *S*-wave anisotropy. The highest anisotropies in physical properties are usually expected in the finest-grained materials (e.g. Clennell *et al.* 1999) and it seems that this also holds in terms of ultrasonic properties in the smectite-rich Muderong Shale. Coarser-grained clay minerals such as kaolinite have been documented to have lower anisotropies than those observed in the Muderong Shale (Hornby *et al.* 1997). There is also likely to be a significant contribution to the anisotropy in the Muderong Shale from the presence of microcracks, especially seen in the *S*-wave velocity. Differences in the response of *S*-wave anisotropy are noted under isotropic and anisotropic stress conditions (*cf.* Figs 9 and 12). Under isotropic stress conditions (Fig. 12), cracks present in the Muderong Shale (Fig. 1) will close and this causes a significant decrease in ultrasonic anisotropy at low stress levels (~5 MPa). However, under anisotropic stress conditions (Fig. 9) with maximum stress parallel to the crack orientation, cracks are ideally oriented to remain open (e.g. Paterson 1978; Jaeger & Cook 1979). In this case, isotropic confining pressure serves to close cracks, while application of differential stress parallel to the cracks tends to open them, resulting in high anisotropy which decreases slowly with increasing mean effective stress. This also suggests that isotropic stress changes have more effect on crack-induced anisotropy than differential stress does (e.g. Fig. 10). Jakobsen & Johansen (2000) also note the decrease of ε with increasing isotropic stress and further decrease with the application of axial load; γ was relatively unchanged in their experiments. Kerogen has also been implicated as a source of high anisotropy in shales (Johnston 1987; Vernik & Liu 1997); in the case of the Muderong Shale, TOC is <0.5 per cent and only small isolated particles of organic matter are visible under the SEM (Dewhurst *et al.* 2002a), likely ruling this out as a significant contributor to the observed anisotropy.

Differential stress

Part of the rationale for these tests was to determine which stress velocity responds to and further to that, the effect that increasing differential stress (i.e. increasing stress anisotropy) has on ultrasonic properties. Given that the orientation of the core was cut such that axial stress was parallel to the microfabric (bedding), this simulated the effects of increasing horizontal (tectonic) stress on ultrasonic properties. In tectonically stressed areas, it is difficult to predict pore pressure from velocity alone, as there is no relationship between vertical stress and velocity, while porosity often does not change (e.g. Yassir 1998; Hennig *et al.* 2002). Harrold *et al.* (1999) emphasized that pore pressure prediction should use wherever possible the mean effective stress, rather than vertical effective stress, in order to reduce errors and uncertainty. However, this also depends on whether a rock mass is intact or fractured as fractures significantly affect velocity and elastic properties (e.g. Sayers 1999). Our study supports the Harrold *et al.* (1999) findings in that the velocity responds smoothly to the mean effective stress alone, rather than vertical effective stress (nett pressure in these experiments), even in a shale containing fractures (*cf.* Figs 6 and 10).

Sonic log velocities are often used to estimate uplift in areas with high horizontal stresses (Densley *et al.* 2000; van Ruth & Hillis 2000) and rely on finding wells with little uplift history for comparison. One of the difficulties with this type of approach though is that high horizontal stresses tend to increase velocity at any given vertical effective stress (or depth). Fig. 10 shows that even with relatively low stress anisotropy ($\sigma'_1 - \sigma'_3$ rising from 0.5 to 8 MPa), velocity is increased by up to 100 m s^{-1} from that seen in the isotropic stress state (again, nett pressure is roughly equivalent to vertical effective stress in this scenario). Given that increasing stress anisotropy also increases velocity parallel to the maximum stress orientation, care should be taken in using such approaches to delimit uplift.

CONCLUSIONS

The Muderong Shale was tested ultrasonically in a changing stress field simulating undrained tectonic deformation. An important result of this study is that velocities in this shale (both *P* and *S* wave) and c_{ij}'s only responded in a monotonic fashion to changes in mean effective stress, rather than changes in nett pressure (equivalent to vertical effective stress in these tests). Pore pressure prediction usually assumes that vertical stress is the maximum principal stress and ignores the effect of horizontal stress. However, even at the low levels of differential stress attained in these tests, significant velocity changes were noted. V_p/V_s ratios in smectite-rich shales are high intrinsically and appear to increase with increasing mean effective stress below ~25 MPa, but decreases at higher stress levels. High intrinsic V_p/V_s ratios are likely due to the presence of smectite, which has water in its mineral structure and decreases in V_p/V_s ratio may be due to stress induced dewatering of smectite.

The Muderong Shale also has a high degree of innate anisotropy resulting from its fine grain size, strong compaction fabric, composition (interlayer water in smectite) and the presence of stress relief microfractures in core. Changes in ultrasonic anisotropy occur primarily as a result of changes in the magnitude of the mean effective stress, as well as the orientation and degree of anisotropy of the stress field. Increasing mean effective stress generally decreases ultrasonic anisotropy but this decrease is also dependent on the degree of stress anisotropy. Decreases in ultrasonic anisotropy are more marked in a changing isotropic stress field, than a changing anisotropic stress field. Changes in differential stress (stress anisotropy) do not appear to affect *P*-wave and *S*-wave anisotropy at given levels of nett pressure (vertical effective stress). The results show that care should be taken when using standardized and isotropic approaches when dealing with compacted smectite-rich

shales due to their highly anisotropic nature and likely compositional effects on velocity.

ACKNOWLEDGMENTS

We are indebted to ChevronTexaco's Australian Business Unit (especially Matthew Johnson) for supplying the shale core used in these tests. The help of Bruce Maney in CSIRO's rock mechanics facility is also duly noted. Bernhard Krooss of the University of Aachen kindly provided the permeability measurement on Muderong Shale. This work was performed under the aegis of the Abnormal Geopressure Programme in the Australian Petroleum Co-operative Research Centre. Sponsors of this programme were ChevronTexaco, Schlumberger and BHP-Billiton. Xiuming Wang is thanked for running the model described in Fig. 4. Milovan Urosevic and Boris Gurevich of Curtin University are thanked for helpful discussions on the finer points of geophysics. Colin Sayers, an anonymous reviewer plus editor Thorsten Becker provided thoroughly constructive and insightful comments that improved the original manuscript considerably.

REFERENCES

Atkinson, J.H. & Bransby, P.L., 1978. *The Mechanics of Soils—An Introduction to Critical State Soil Mechanics*, McGraw-Hill, London, 375pp.

Banik, N.C., 1984. Velocity anisotropy of shales and depth estimation in the North Sea basin, *Geophysics,* **49,** 1411–1419.

Biot, M. & Willis, D.G., 1957. The elastic coefficients of the theory of consolidation, *Journal of Applied Mechanics,* **24,** 594–601.

Carrion, P., Costa, J., Pinheiro, J.E.F. & Schoenberg, M., 1992. Cross-borehole tomography in anisotropic media, *Geophysics,* **57,** 1194–1198.

Clennell, M.B., Dewhurst, D.N., Brown, K.M. & Westbrook, G.K., 1999. Permeability anisotropy of consolidated clays, in *Muds and mudstones: physical and fluid flow properties*, Vol. 158, pp. 79–96, eds Aplin, A.C., Fleet, A.J. & Macquaker, J.H.S. Geological Society of London Special Publication.

Dellinger, J. & Vernik, L., 1994. Do travel times in pulse transmission experiments yield anisotropic group or phase velocities?, *Geophysics,* **59,** 1774–1779.

Densley, M.R., Hillis, R.R. & Redfearn, J.E.P., 2000. Quantification of uplift in the Carnarvon Basin based on interval velocities, *Australian Journal of Earth Sciences,* **47,** 111–122.

Dewhurst, D.N. & Hennig, A., 2003. Geomechanical properties related to top seal leakage in the Carnarvon Basin, Northwest Shelf, Australia, *Petroleum Geoscience,* **9,** 255–263.

Dewhurst, D.N., Jones, R.M. & Raven, M.D., 2002a. Microstructural and petrophysical characterisation of Muderong Shale: application to top seal risking. *Petroleum Geoscience,* **8,** 371–383.

Dewhurst, D.N., Raven, M.D., van Ruth, P., Tingate, P.R. & Siggins, A.F., 2002b. Acoustic properties of Muderong Shale, *APPEA Journal,* **42,** 241–57.

Dewhurst, D.N., Aplin, A.C. & Sarda. J.P., 1999a. Influence of clay fraction on pore-scale properties and hydraulic conductivity of experimentally compacted mudstones, *Journal of Geophysical Research, Solid Earth,* **104/B12,** 29 261–29 274.

Dewhurst, D.N., Yang, Y. & Aplin, A.C., 1999b. Fluid flow through natural mudstones, in *Muds and mudstones: physical and fluid flow properties*, Vol. 158, pp. 23–43, eds Aplin, A.C., Fleet, A.J. & Macquaker, J.H.S., Geological Society of London Special Publication.

Dewhurst, D.N., Aplin, A.C., Sarda, J.-P. & Yang, Y., 1998. Compaction-driven evolution of porosity and permeability in natural mudstones: an experimental study, *Journal of Geophysical Research, Solid Earth,* **103/B1,** 651–661.

Domnesteanu, P., McCann, C. & Sothcott, J., 2002. Velocity anisotropy and attenuation of shale in under- and overpressured conditions, *Geophys. Prospect.,* **50,** 487–503.

Fjær, E., Holt, R.M., Horsrud, P., Raaen, A.M. & Risnes, R., 1992. Petroleum Related Rock Mechanics, *Developments in Petroleum Science,* 33, Elsevier, Amsterdam, 338 pp.

Fitts, T.G. & Brown, K.M., 1999. Stress-induced smectite dehydration: ramifications for patterns of freshening and fluid expulsion in the N. Barbados accretionary wedge, *Earth planet. Sci. Lett.,* **172,** 179–197.

Harrold, T.W.D., Swarbrick, R.E. & Goulty, N.R., 1999. Pore pressure estimation from mudrock porosities in Tertiary basins, southeast Asia, *AAPG Bulletin,* **83,** 1057–1067.

Hatchell, P.J., van den Beukel, A., Molenaar, M.M., Maron, K.P., Kenter, C.J., Stammeijer, J.G.F., van der Velde, J.J. & Sayers, C.M., 2003. Whole earth 4D: monitoring geomechanics. Proceedings of the Society of Exploration Geophysicists 73rd Annual Meeting, Expanded Abstracts, 4pp.

Helbig, K. & Schoenberg, M., 1987. Anomalous polarisation of elastic waves in transversely isotropic media, *Journal of the Acoustic Society of America,* **81,** 1235–1245.

Hennig, A., Yassir, N., Addis, M.A. & Warrington, A., 2002. Pore pressure estimation in an active thrust region and its impact on exploration and drilling, in *Pressure Regimes in Sedimentary Basins and Their Prediction*, Vol. 76, pp. 89–105, eds Huffman, A. & Bowers, G., American Association of Petroleum Geologists Memoir.

Holt, R.M., Fjær, E. & Rzayev, E., 2004. P- and S-wave velocities in shales: experiments and a model. Proceedings of the 6th North American Rock Mechanics Symposium (Gulf Rocks 2004), ARMA/NARMS paper no 04–543, 8pp.

Holt, R.M., Fjær, E., Raaen, A.M. & Ringstad, C., 1991. Influence of stress state and stress history on acoustic wave propagation in sedimentary rocks, in *Shear Waves in Marine Sediments*, pp. 167–74, eds Hovem, J.M., Richardson, M.D. & Stoll, R.D., Kluwer, The Netherlands.

Hornby, B.E., 1998. Experimental laboratory determination of the dynamic elastic properties of wet, drained shales, *J. geophys. Res.,* **103/B12,** 29 945–964.

Hornby, B.E., Johnson, C.D., Cook, J.M. & Coyner, K.S., 1997. Experimental determination of the elastic properties of a compacting sediment. Proceedings of the Society of Exploration Geophysicists 67th Annual Meeting, Expanded Abstracts, 4 p.

Horsrud, P., Sønstebø, E.F. & Bøe, R., 1998. Mechanical and petrophysical properties of North Sea shales, *Int. J. Rock Mech. Min. Sci.,* **35,** 1009–1020.

Jaeger, J.C. & Cook, N.G.W., 1979. *Fundamentals of Rock Mechanics*, 3rd edn, Chapman & Hall, London, 591 pp.

Jakobsen, M. & Johansen, T.A., 2000. Anisotropic approximations for mudrocks: a seismic laboratory study, *Geophysics,* **65,** 1711–1725.

Johnston, J.E. & Christensen, N.I., 1995. Seismic anisotropy of shales, *J. geophys. Res.,* **100,** 5991–6003.

Johnston, J.E. & Christensen, N.I., 1994. Elastic constants and velocity surfaces of indurated anisotropic shales, *Surv. Geophys.,* **15,** 481–494.

Johnston, D.H., 1987. Physical properties of shales at temperature and pressure, *Geophysics,* **52,** 1391–1401.

Jones, L.E.A. & Wang, H.F., 1981. Ultrasonic velocities in Cretaceous shales from the Williston Basin, *Geophysics,* **46,** 288–297.

Katsube, T.J., Mudford, B.S. & Best, M.E., 1991. Petrophysical characteristics of shales from the Scotian shelf, *Geophysics,* **56,** 1681–1689.

Kenter, C.J., van den Beukel, A., Hatchell, P.J., Maron, K.P., Molenaar, M.M. & Stammeijer, J.G.F., 2004. Geomechanics and 4D: evaluation of reservoir characteristics from time shifts in the overburden. Proceedings of the 6th North American Rock Mechanics Symposium (Gulf Rocks 2004), ARMA/NARMS paper no. 04–627, 7 p.

Lal, M., 1999. *Shale stability: drilling fluid interaction and shale strength*, SPE paper number 54356, 10 p.

Lekhnitskii, S.G., 1981. *Theory of Elasticity of an Anisotropic Body*, Mir Publishers, Moscow, 430 p.

Mavko, G. & Mukerji, T., 1998. Bounds on low-frequency seismic velocities in partially saturated rock, *Geophysics,* **63,** 918–924.

Meadows, M.A. & Abriel, W.L., 1994. 3-D post-stack phase-shift migration in transversely isotropic media. Proceedings of the Society of Exploration Geophysicists, 64th Annual Meeting, Expanded Abstracts, 1205–1208.

Molenaar, M.M., Hatchell, P.J., van den Beukel, A.C., Jenvey, N.J., Stammeijer, J.G.F., van der Velde, J.J. & de Haas, W.O., 2004. Applying geomechanics and 4D: '4D in situ stress' as a complementary tool for optimizing field management. Proceedings of the 6th North American Rock Mechanics Symposium (Gulf Rocks 2004), ARMA/NARMS paper no 04–639, 8 p.

Paterson, M.S., 1978. *Experimental Rock Deformation: The Brittle Field*, Springer-Verlag, New York, 254 p.

Sayers, C.M., 1999. Stress-dependent seismic anisotropy of shales, *Geophysics,* **64,** 93–98.

Sayers, C.M. & Ebrom, D., 1997. Seismic traveltime analysis for azimuthally anisotropic media: Theory and experiment, *Geophysics,* **62,** 1570–1582.

Sayers, C.M., Woodward, M.J. & Bartman, R., 2001. Pre-drill pore pressure prediction using 4C seismic, *The Leading Edge,* **20,** 1056–1059.

Sheriff, R.E., 2002. Encyclopedic dictionary of applied geophysics. Geophysical Reference Series, 13. Society of Exploration Geophysicists, Tulsa, Oklahoma, 429 p.

Siggins, A.F. & Dewhurst, D.N., 2003. Saturation, Pore Pressure and Effective Stress from Sandstone Acoustic Properties, *Geophys. Res. Lett.,* **30**(2), Article no. 1089.

Skempton, A.W., 1954. The pore pressure coefficients A and B, *Geotechnique,* **4,** 143–147.

Thomsen, L., 1986. Weak elastic anisotropy, *Geophysics,* **51,** 1954–1966.

Tsvankin, I., 2001. *Seismic Signatures and analysis of Reflection Data in Anisotropic Media*, Pergamon Press, Amsterdam, 436 p.

van Ruth, P. & Hillis, R., 2000. Estimating pore pressure in the Cooper Basin, South Australia; sonic log method in an uplifted basin, *Exploration Geophysics,* **31**(1–2), 441–447.

Vernik, L. & Liu, X., 1997. Velocity anisotropy in shales; a petrophysical study, *Geophysics,* **62,** 521–532.

Vernik, L. & Landis, C., 1996. Elastic anisotropy of source rocks: Implications for hydrocarbon generation and primary migration, *Bulletin of the American Association of Petroleum Geologists,* **80,** 531–544.

Vernik, L. & Nur, A., 1992. Ultrasonic velocity and anisotropy of hydrocarbon source rocks, *Geophysics,* **57,** 727–735.

Wang, X., 2001. Seismic wave simulation in anisotropic media with heterogeneity using a high-order finite difference method. Proceedings of the 5th SEGJ International Symposium, 113–120.

Wang, Z., 2002a, Seismic anisotropy in sedimentary rocks, part 2: Laboratory data, *Geophysics,* **67,** 1423–1440.

Wang, Z., 2002b, Seismic anisotropy in sedimentary rocks, part 1: A single plug laboratory method, *Geophysics,* **67,** 1415–1422.

Wright, J., 1987. The effects of transverse isotropy on reflection amplitude verus offset, *Geophysics,* **52,** 564–567.

Yassir, N., 1998. Overpressuring in compressional regimes—causes and detection, in *Overpressures in Petroleum Exploration*, pp. 13–18, eds Mitchell, A. & Grauls, D., Bulletin Recherche Elf Exploration and production, Memoir 22.